The following article appeared in Applied Surface Science Advances, Volume 13, February 2023, 100378 and may be found at: https://doi.org/10.1016/j.apsadv.2023.100378

Applied Surface Science Advances 13 (2023) 100378

Contents lists available at ScienceDirect

Applied Surface Science Advances

journal homepage: www.sciencedirect.com/journal/applied-surface-science-advances

A functional SiO_2-TiO_2 mesoporous assembly designed for the controlled release of carvacrol

T.A. Esquivel-Castro, G. Robledo-Trujillo, J. Oliva, H.C. Rosu, V. Rodríguez-González *

Instituto Potosino de Investigación Científica y Tecnológica (IPICyT), División de Materiales Avanzados, Camino a la presa San José 2055, Col. Lomas 4a sección, San Luis Potosí, SLP 78216, Mexico

ARTICLE INFO

Keywords:
Drug delivery
Carvacrol
Mesoporous architecture
SiO_2-TiO_2 composite
Triethanolamine
Spherical-like assembly

ABSTRACT

Mesoporous composites can be useful for the gentle release of biocides and fertilizers. Here, we study the structural, morphological, and drug-delivery advantages of SiO_2-TiO_2 (PST) particles synthesized by a hydrothermal method. The PST particles had a spherical-like assembly architecture, which was obtained by cobalt ions incorporation. Each assembly contains nanobars with acute or obtuse tip shape, notably in the sample with 0.5 wt% of Co. Drug loading/delivery evaluations were carried out using carvacrol (CVC) as biocidal molecule. PST composites functionalized with the triethanolamine presented higher load efficiencies of 30–37% and load capacities of 20–26%. A similar trend occurred for the release percentage of CVC. The PST samples without functionalization had a release of only 19–29% (at pH=7.4). After the TEOA functionalization, the release percentage was enhanced to 64–78%. Moreover, the PST had a maximum release percentage of 64.8% reached after only 3 min (at pH=7.4). In contrast, the PST doped with 1 wt% of Co reached the maximum release percentage of 64.8% after 24 h at pH=7.4. Hence, the results of this investigation demonstrate that the PST synthetized with Co and functionalized with TEOA could be used for the control of undesired weed and phytopathogens in cultivated plants by prolonging their delivery time of biocidal molecules.

1. Introduction

The high growth of the human population has generated a strong increase in the pollution of the environment which became a very serious issue [1]. During the last decade, nanotechnology has gained importance as a tool to solve menacing environmental problems such as [2]: contamination of water sources by heavy metals and dyes [3–5], as well as the contamination of the soil and air by agrochemicals and fertilizers [6–10]. In order to promote the sustainable agriculture, nanomaterials have been used as vehicles for the release of biomolecules, agrochemicals or nutrients that help the growth of the plants [11–13] and to the control of diseases caused by bacteria, fungi, viruses, etc. [11, 14-17]. Therefore, nanomaterials with high specific surface area/-volume ratio are suitable to be loaded with herbicides/pesticides, which in turn, are employed for the protection and growth of crops.

On the other hand, natural biocide molecules can be used in agriculture due to their antifungal and antimicrobial properties. Among them, the Carvacrol (5-isopropyl-2-methylphenol) is a phenolic monoterpene, which possesses natural antimicrobial properties, and it is extracted from the oregano [18]. In fact, Carvacrol has been reported to inhibit the growth of foodborne pathogens (*Staphylococcus aureus*) and shows microbial activity against gram-positive microorganisms [19] and *Escherichia coli* [20]. In addition, the Carvacrol exhibits antioxidant, antibacterial, antifungal, antiviral, anti-inflammatory and anticancer properties [21,22]. Due to those last properties, the Carvacrol (CVC) has been used for the pest control (herbicide) in small crop areas, but its wide agricultural use is limited by its sensitivity to light, humidity, temperature, and low solubility in water [20]. One way to solve the last issues is encapsulating the CVC into porous nanoparticles in such a way that it is protected from the environment and could be slowly released. The load of CVC in inorganic matrices is hard to achieve in general, hence few articles have been reported about the employment of ceramic matrices as vehicles for the release of carvacrol for applications in agriculture. For example, Altan et al. [23] reported the encapsulation of carvacrol in ultrafine zein fibers with tributyl citrate using the electrospinning technique. They obtained encapsulation efficiencies of 40–81% depending on the concentration of zein and carvacrol. The highest encapsulation efficiency was reached for a zein concentration of 36% and 7% of CVC, while the lowest encapsulation efficiency was obtained for a zein concentration of 32.1% and 4% of CVC. Thus, the increase in the concentration of zein increases the encapsulation efficiency of CVC

* Corresponding author.
E-mail addresses: hcr@ipicyt.edu.mx (H.C. Rosu), vicente.rdz@ipicyt.edu.mx (V. Rodríguez-González).

https://doi.org/10.1016/j.apsadv.2023.100378
Received 2 September 2022; Received in revised form 15 January 2023; Accepted 15 January 2023
Available online 20 January 2023

Abbreviation definition

PST	SiO_2-TiO_2 composite
CVC	Carvacrol
TEOA	Triethanolamine
HC	Hydrophobic chitosan
NPs	Nanoparticles
ROS	Reactive oxygen species
TEOS	Tetraethyl orthosilicate
TTIP	Titanium (IV) isopropoxide
P-123	Poly(ethylene glycol)-block-poly(propylene glycol)-block-poly(ethylene glycol)
HCl	Hydrochloric acid
EtOH	Ethanol
Co	Cobalt
LE%	Load efficiency
LC%	Load capacity
PBS	Phosphate buffered saline solution
UV–Vis	Ultraviolet-visible
BET	Brunauer-Emmet-Teller
SEM	Scanning Electron Microscope
EDS	Energy dispersive X-ray spectroscopy
ICP	Inductively Coupled Plasma (ICP-OES)
XRD	X-ray diffraction
D	Crystallite size
λ	Wavelength of X-ray radiation
k	Constant
β	Line width at half maximum height
θ	Diffraction angle
X_R	Weight fraction of rutile
I_R	Relative intensities of rutile
I_A	Relative intensities of anatase
BJH	Barrett-Joyner-Halenda
FTIR	Fourier Transform Infrared Spectroscopy
ATR	Attenuated total reflectance
FESEM	Field Emission Scanning Electron Microscope
IUPAC	International Union of Pure and Applied Chemistry
Vp	Total pore volume

in the fibers. Hydrophobic chitosan (HC) nanoparticles (NPs) modified with octanoic acid have also been used for CVC loading [24]. Those NPs were synthesized using the ionotropic gelation approach. The CVC was loaded on these particles at concentrations of 25%, 50% and 75%. Consequently, the encapsulation efficiencies of 36.8, 56.4 and 19.3% have been obtained, respectively. Regarding the% of load capacity, the HC NPs reached a maximum loading efficiency of 21.9% with 1.40 mg of CVC, showing a saturation in the system. Thus, the hydrophobic character of the NPs allows a better retention of CVC. The authors also demonstrated that the HCs NPs released 11% of the encapsulated CVC after 250 min, while the pure chitosan NPs released 40% of the CVC in 110 min. Also, the CVC has been loaded onto beta cyclodextrin-alginate-chitosan nanoflowers by Salari et al. [25] who have found that the highest loading capacity of carvacrol was 96.63%. The release was carried out in a dialysis bag using phosphate buffer at pH 3.0 and 6.0. Ethanol was employed as the receptor solution. They observed that at pH 3.0 > 90% was released after 300 min, while at pH 6.0 the same amount was released in only 120 min. This occurred because the swelling of the polymeric matrix in the acidic medium is faster [25]. Hence, the reports above demonstrate that the CVC can be encapsulated in porous materials and still present antibacterial activity.

Due to the low efficiency to load or to release the CVC, it is still necessary to develop materials with excellent characteristics such as large surface area, ideally with mesoporosity, having controllable pore volume, and functionalizable surface for a higher loading capacity of drugs or natural molecules. For this purpose, in this work, we synthesized mesoporous cobalt doped SiO_2-TiO_2 composites for the loading and release of CVC. The silicon dioxide was selected because it has good chemical and mechanical stability, as well as a surface area above 300 m^2/g with good biocompatibility [26]. On the other hand, TiO_2 is considered one of the best catalysts and its photocatalytic performance depends on the size and crystalline phase of the nanoparticles [27]. Additionally, the TiO_2 causes photocatalytic disinfection or inactivation of microorganisms, due to the reactive oxygen species (ROS) that are generated on the surface of the material causing a damage on the cell membrane [27]. Furthermore, it has been reported that doping TiO_2 with some metallic ions, such as Li^+, Ag^+, Co^{2+} and Cu^{2+}, enhances and/or diversifies the antibiocidal properties [28]. For instance, Basiron et al. [29] showed that the TiO_2:Li/Polyethylene composite produced an enhanced adsorption of water, which increased its capacity for the generation of ROS for the inactivation of the *S. aureus* bacteria. To the best of our knowledge, the mesoporous SiO_2-TiO_2 composite has not been employed as a CVC delivering system. For this reason, the loading/release performance of this composite for the CVC molecule administration was evaluated. First, the effect of cobalt-incorporation SiO_2-TiO_2 (PST) on the architecture of composites was characterized. In order to enhance the loading capacity of PST, the surface functionalization with triethanolamine (TEOA) was carried out with the effect of a loading capacity increase of up to 20–25.4%. Moreover, the release efficiency of the PST-TEOA composites was evaluated at pH 3 and 7.4 and it was found a maximum release of 77.4% (after 24 h) obtained for the SiO_2-TiO_2-TEOA composite with 1% Co. Thus, the results of this work indicate that our SiO_2-TiO_2 composites functionalized with TEOA are a good alternative for the load and release of CVC. This material loaded with CVC could find application in sustainable agriculture for the weed inactivation.

2. Experimental

2.1. Materials

All the reagents: Tetraethyl orthosilicate (TEOS) (Aldrich, 98%), titanium (IV) isopropoxide (TTIP) (Aldrich, 97%), Pluronic P-123 (Poly (ethylene glycol)-block-poly(propylene glycol)-block-poly(ethylene glycol), Aldrich), cobalt (II) nitrate hexahydrate (Aldrich, 98%), HCl (J. T. Baker, 36.5–38%), triethanolamine (TEOA) (CTR Scientific, 99.97%) ethanol (Karal, 96%), and distilled water as well as the Carvacrol (Aldrich, 98%, biocide molecule) were used as received and without further treatment.

2.2. Synthesis of the undoped and Co doped SiO_2-TiO_2 composites

In a typical synthesis: 2.66 g of Pluronic P-123 were dissolved in 10 mL of distilled water. Next, a 2 M HCl solution was prepared and poured into a hydrothermal reactor and the Pluronic P-123 was added by slow dropping during 5 h at 40 °C. After that, 12 g of TEOS are added dropwise keeping 600 rpm of constant stirring. Afterwards, a certain amount of Cobalt (II) nitrate hexahydrate (it depended on the desired Co concentration 0.5% or 1 wt%) was dissolved in 10 mL of distilled water. Later, 6 g of TTIP and the cobalt solution were added at the same time in the mixture solution containing TEOS + Pluronic P-123. Once these solutions are added, the reactor is closed and maintained at 40 °C for 24 h. Subsequently, the microwave-assisted hydrothermal process was carried out at 150 W and 100 °C for 6 h. After this, the reactor was cooled down at room temperature and the precipitated powder was recovered by vacuum filtration.

The as prepared powders were annealed at 600 °C for 5 h. The samples synthesized with 0.5 and 1 wt% of Co were named PST 0.5% Co and PST 1% Co, respectively. The reference sample synthesized without Co incorporation was named as PST.

2.3. Surface functionalization of SiO_2-TiO_2 composites with triethanolamine

The surface functionalization of the composites was carried out using a method previously reported [30]. For this procedure 0.1 g of PST powder were added to 50 mL of distilled water. Subsequently, 1 mL of TEOA was added to the solution and stirred for 30 min. Next, the solution was placed in a water bath at 90 °C for 3 h. The powders functionalized with TEOA were centrifuged at 4000 rpm for 30 min and washed 3 times with distilled water and ethanol in order to eliminate the possible non stable or in excess TEOA. After this, the powders have been dried at 60 °C for 12 h. The undoped PST powder functionalized with triethanolamine (TEOA) was named as PST/TEOA. The Co synthetized PST powders functionalized with TEOA were named as PST 0.5% Co/TEOA and PST 1% Co/TEOA. Table ST1 in supporting information presents the description of each sample studied in this work.

2.4. Loading of carvacrol on functionalized SiO_2-TiO_2 composites

The loading of CVC on the undoped and Co doped PST composites was achieved through the adsorption/impregnation method. Firstly, a stock solution of CVC in ethanol was prepared at a concentration of 500 mg L^{-1}. Next, 10 mL of the stock solution was kept at 25 °C in darkness for 48 h. The loading of the samples with CVC was carried out in triplicate. Afterwards, the impregnated powder was separated from the liquid by centrifugation and its absorbance measured at a wavelength of 276 nm. The load efficiency (LE%) and the load capacity (LC%) was calculated using the following equations. The calibration curves employed is shown in the Figure S1 of the supporting information.

$$\text{LE\%} = \frac{\text{Amount of CVC adsorbed (mg)}}{\text{Initial CVC (mg)}} \text{X } 100 \tag{1}$$

$$\text{LC\%} = \frac{\text{Amount of CVC adsorbed (mg)}}{\text{SiO}_2 - \text{TiO}_2 \text{ composite (mg)}} \text{X } 100 \tag{2}$$

For this work, the initial CVC quantity was 5 mg (Eq. (1)) and 10 mg (Eq. (2)) for the SiO_2-TiO_2 composite.

2.5. In-vitro release of carvacrol

The CVC release was carried out using 5 mg of loaded PST powder (without or with Co) in 15 mL of dissolution medium. In this case, the dissolution medium was a phosphate buffered saline solution (PBS) at pH of 7.4 and hydrochloric acid solution at a pH of 3.0. The PST samples loaded with CVC were kept in the incubator at 37 °C. In order to perform a release kinetics, 1 mL aliquots were taken at different time intervals of 3, 6, 9, 12, 15, 30 min, 1 h, 2 h, 4 h, 6 h, 8 h and 24 h. Next, the absorbance value at a wavelength of 273 nm was determined for each aliquot using a UV–Vis spectrophotometer. For the calibration curve for CVC in PBS, see Figure S2 in the supporting information, and the following equation was employed to obtain the cumulative release percentage of CVC:

$$\text{Release\%} = \sum_{i=3\ \text{min}}^{24\ \text{h}} \frac{\text{Released carvacrol on time} = i\ \text{(mg)}}{\text{Initial carvacrol (mg)}} \text{X } 100 \tag{3}$$

Finally, we should mention that all the kinetic experiments were carried out by triplicate for each sample.

Several mathematical models were evaluated to understand and describe the release mechanism of carvacrol in PST composites without Co and with Co, as well as composites that have been surface-modified with triethanolamine (TEOA), (see supporting information).

2.6. Morphological, structural, and BET characterizations

The morphology of the SiO_2-TiO_2 composites synthesized with and without cobalt incorporation were analyzed by scanning electron microscopy (SEM). For this purpose, the FEI-FIB Helios Nanolab microscope was employed at 5–8 kV. The energy dispersive X-ray spectroscopy (EDS) spectra were recorded by using a Thermo-scientific detector coupled to the SEM microscope. The X-ray diffraction (XRD) patterns were obtained using a diffractometer D8 Advance model, Bruker equipment, with the Cu-Kα radiation of 1.5418 Å. The XRD patterns were recorded in the range 5–90° (2θ) at increments of 0.01° with a sweep time of 0.1 s. The crystallite size was estimated by the Scherrer's equation at the most intense peak of the anatase (101) and rutile phase (110):

$$D = \frac{\text{K}\lambda}{\beta \cos\theta} \tag{4}$$

where D is the crystallite size in Å, λ is the wavelength of X-ray radiation (Å), K is a constant for which usually the value of 0.89 is taken, β is the line width at half maximum height in radians and θ is the diffraction angle in degrees. The phase composition was also calculated using the following equation [31]:

$$X_R = 1 - \left(\frac{1}{1 + 1.26\left(\frac{I_R}{I_A}\right)} \right) \tag{5}$$

where X_R is the weight fraction of rutile, I_R and I_A are the relative intensities of the most intense diffraction peak of rutile and anatase, respectively.

The specific surface area of SiO_2-TiO_2 composites with and without cobalt was determined by N_2 adsorption-desorption isotherms using a Quantachrome Instruments, Nova 3200e model and NovaWin software (Quantachrome Instruments). The samples were degassed at 120 °C for 20 h before the BET measurements. The specific surface area was calculated according to Brunauer-Emmet-Teller (BET) method and the pore size distributions were calculated according to the Barrett-Joyner-Halenda (BJH) model using the nitrogen desorption isotherm.

2.7. Optical characterization

The Fourier Transform Infrared (FTIR) spectra were recorded in a range of 4000 to 400 cm^{-1}, using a Shimadzu IR-Tracer spectrophotometer and the ATR accessory. The UV–vis absorption presented in this research were measured in the range of 200 to 400 nm using a UV–Vis Agilent Cary 5000 spectrophotometer.

3. Results and discussion

3.1. Effect of the Co concentration on the morphology and structure of SiO_2-TiO_2 composites

Fig. 1a shows the morphology of the PST, where nanoparticles with flake-like morphology and overlapping flake structure are observed. A closer view of the quasi-flake is depicted in the Fig. 1b, see the yellow circles and some appear as flattened bars. The flake-like nanoparticles have sizes from 90 to 125 nm, see the circle with cyan color in the Fig. 1a. The average size distribution of the flake-like nanoparticles was determined using the ImageJ software, obtaining a size of 93 ± 32 nm (inset Fig. 1a). The Fig. 1b also shows particles with flattened bars shape, which have sizes of 135–192 nm. In addition, some holes or apertures between the flakes are visualized in the agglomeration of flake-like nanoparticles, not well assembled. Fig. 1c shows the morphology of

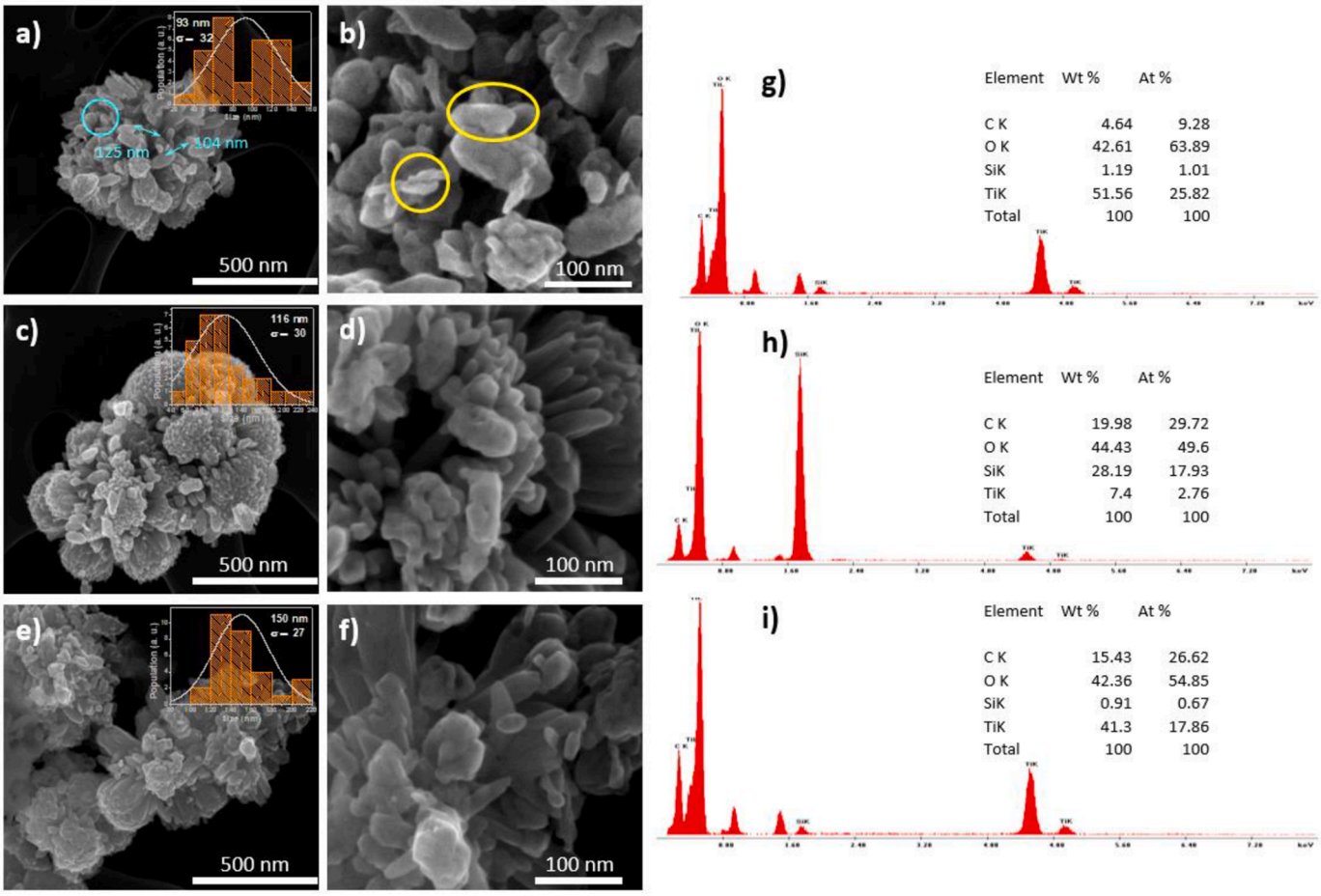

Fig. 1. SEM images of: (a-b) PST, (c-d) PST 0.5%, (e-f) PST 1% Co composites. EDX results of (g) PST, (h) PST 0.5% Co and (i) PST 1% Co composites.

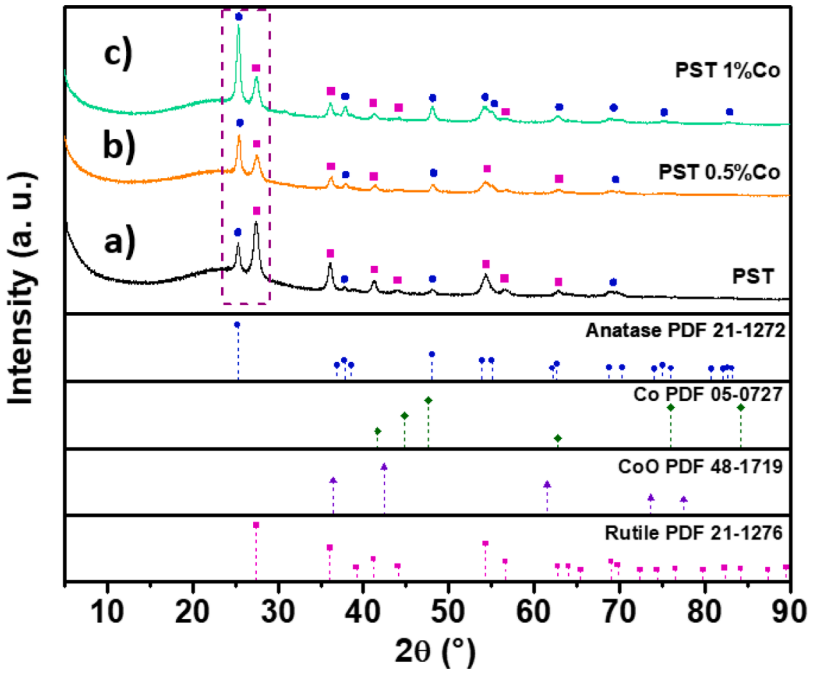

Fig. 2. XRD patterns for the undoped and Co doped PST composites.

the PST composite with 0.5 wt% of Co. There are layered cumulations with average size of 237 nm, which contain well defined nanobars with average size distribution of 116 ± 30 nm (inset Fig. 1c). It seems that hydrothermal environments in the presence of cobalt ions allows to obtain spherical-like agglomerated assemblies of diverse diameters. Each assembly is composed of nanobars with acute or obtuse tip shape, see the Fig. 1d. Fig. 1e shows the morphology of the PST composite with 1 wt% of cobalt. Again, flattened bars particles mixed with nanorbars were observed. The diverse shaped particles and the nanobars have an average size of 67 and 150 ± 27 nm, respectively. The average size distribution of the nanobars is shown in the inset of Fig. 1e. Based on the analysis of the morphology with the FESEM images, increasing the cobalt concentration raises the size of the agglomerates and nanobars. The morphology of the spherical assembly is better visualized in the PST with a 0.5 wt% of Co. Fig. 1g, 1h and 1i show the EDX analysis of the PST, PST 0.5% Co and PST 1% Co samples where it can be seen that the SiO_2-TiO_2 composites are composed of Si, Ti, O and C. It should be mentioned that the presence of cobalt is not observed in the 0.5% and 1% PST samples because the amount of cobalt is small (0.5 wt% and 1 wt %) and it is not detected by the equipment.

The XRD patterns reveal that all samples (PST, PST 0.5% Co, and PST 1% Co) present a combination of anatase phase (JCPDS 21–1272) and the rutile (JCPDS 21–1276) TiO_2 phases [32], see the XRD pattern 2a on Fig. 2. The broad peak that extends from 15 to 30° is attributed to a low crystalline SiO_2 phase in the composite (01–75–3162), low crystalline silica synthesized by sol-gel in contrast with the cristobalite beta crystalline phase (04–007–2134). However, with lower intensity and broadening we have the anatase peak at 25.2° This can be attributed to the decrease in the structure of anatase TiO_2 by the modification of Co which leads to the slightly amorphous nature. Also, the PST composite presented mostly a rutile phase since its peak at 27.4° is more intense than that of the anatase phase at 25.2°.

However, the PST samples with cobalt produced a higher content of anatase TiO_2 phase, since the diffraction peak at 25.2° is more intense, see the patterns 2b and 2c. Furthermore, no diffraction peaks related to Co oxides or metallic were observed, indicating that our method of synthesis is good enough to produce SiO_2-TiO_2 composites with spherical assemblies and main anatase crystalline TiO_2 phase. Moreover, there is a displacement toward higher angles for the diffraction peak in all samples (with respect to the reference cards), suggesting a contraction of the lattice. This possibly occurred because the cobalt is interstitial, and it is replacing some titanium in the crystalline lattice (the ionic radius of Co^{+2} is 0.63 Å and that of Ti^{+4} is 0.68 Å [32]) and attaining a Co assembly effect, notable at 0.5% Co.

On the other hand, the crystallite size was calculated with the Scherrer equation and the found values were of 18.76, 16.7 and 17.2 nm for the PST, PST 0.5% Co and PST 1% Co samples, respectively. Thus, a decrease in the crystallite size was observed after introducing the Co dopant in the PST composite. Additionally, the phase composition was determined using the Eq. (5) above. The phase composition for the PST composite was 0.71 for rutile and 0.29 for anatase. The PST 0.5% Co sample had 0.42 rutile and 0.58 anatase and the PST 1% Co sample had 0.32 for rutile and 0.68 for anatase. These results agree well with the intensity of the diffraction peaks observed for the diffraction patterns in the Fig. 2.

3.2. FTIR analysis of SiO_2-TiO_2 and SiO_2-TiO_2:Co composites

Fig. 3 shows the FTIR spectrum of the PST and PST 0.5% Co and PST 1% Co samples. The FTIR spectra reveal a broad band in the range of 3600–3100 cm^{-1}, which is associated to the vibrational stretching mode of the υO—H groups in the water molecule, mainly silanol moiety and hydroxyl surface groups. The band at 1635 cm^{-1} corresponds to the vibrational deformation mode of δ(O—H) groups, silanol and titanol [33]. Other vibrational bands corresponding to the υ_{as}(Si-O-Si) and υ_s(Si-O-H) bonds were observed at 1047 cm^{-1} and 960 cm^{-1} [34],

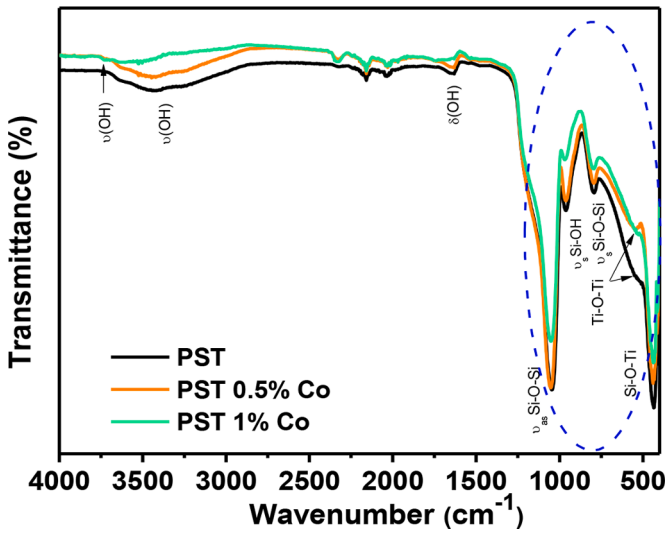

Fig. 3. FTIR spectra for the PST and PST with Co composites.

respectively. Those peaks indicate the existence of a silica framework, where oxygen atoms form bond, superficial and framework siloxanes, also isolated and germinal silanols [34,35]. Similarly, the symmetrical vibration υ_s(Si-O-Si) that appears at 791 cm^{-1} and the bending mode δ(O-Si-O) located at 435 cm^{-1} are characteristic bands of the Si-O-Si. An intense peak located at 433 cm^{-1} was also observed in all samples, which is attributed to the Si-O-Ti bond. Hence, the FTIR spectra indicates the presence of the SiO_2 and TiO_2 interactions materials [34] and blue shift was observed comparing with previous work where only SiO_2 mesoporous was synthetized [36]. According to XRD and FTIR, a mixed oxide SiO_2-TiO_2 framework was considered. In the supplementary material, in Figure S3, it is shown the FTIR spectra of TiO_2 commercial, SiO_2 mesoporous with the sample PST 1% Co, in which one can notice that the band for the hydroxyl moiety is weaker in the PST composites doped with cobalt compared with TiO_2, and additionally the contribution of Ti-O-Ti and Si-O-Ti groups at 1640, 914 and 450 cm^{-1} [33].

3.3. Effect of the Co concentration on the surface area and porosity of SiO_2-TiO_2 composites

The nitrogen gas adsorption-desorption measurements were performed at -185.8 °C (77.35 K). PST and Co-PST samples were degassed at 120 °C for 20 h before each measurement to remove any chemicals or impurities inside pores. Fig. 4a shows the nitrogen adsorption-desorption isotherms for the PST and Co synthetized PST samples. As observed, all the isotherms are type IV according to the IUPAC classification [37], confirming the presence of mesopores and cylindrical pores in the samples. Table 1 presents the textural parameters for the SiO_2-TiO_2 composites. The undoped PST composite had a surface area of 391.7 m^2 g^{-1}, a total pore volume (V_p) of 0.43 cm^3 g^{-1} and a pore diameter of 4.75 nm. After incorporated with 0.5 wt% of cobalt, the surface area increased up to 536.1 m^2 g^{-1}. The total pore volume and pore diameter also increased to 0.67 cm^3 g^{-1} and 5.30 nm, respectively. Thus, introducing the Co produced bigger mesopores [38] as it was observed in FESEM images of a spherical-like assembly. In general, the main pore diameter of the samples is in the size range of mesopores (3–10 nm) [38], see the homogenous size pore size distribution in the Fig. 4b. If the cobalt concentration increases to 1 wt%, all the textural parameters decrease and spherical-like assembly melt due to the flattened bars particles mixed with nanobars, see the Table 1. This behavior was also observed by Pan et al. [39] who synthesized SiO_2-TiO_2 membranes without dopant reporting a surface area of 10.39 m^2 g^{-1}. After adding 0.2 mol% of Pd, the surface area increased to 25.89 m^2 g^{-1}, but it decreased to 21.65 m^2 g^{-1} after adding 0.5 mol% of Pd to the

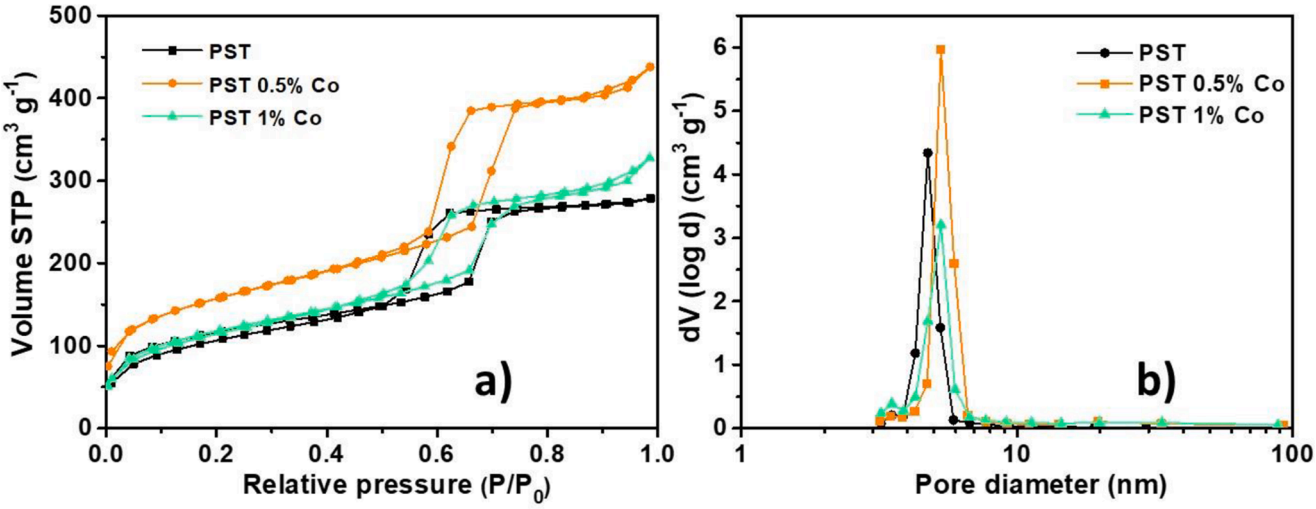

Fig. 4. a) N_2 adsorption-desorption isotherms and b) pore size distribution for the PST and Co synthetized PST composites.

Table 1
Textural properties of the PST and Co-synthesized SiO_2-TiO_2 composites.

Sample	Surface area, S_{BET} ($m^2\ g^{-1}$)	Pore volume, $V_{p\ BJH}$ ($cm^3\ g^{-1}$)	Total pore volume, $V_{total\ pore}$ ($cm^3\ g^{-1}$)	Pore diameter, D_p (nm)
PST	391.7 ± 9	0.38 ± 0.02	0.43 ± 0.07	4.75 ± 0.11
PST 0.5% Co	536.1 ± 12	0.58 ± 0.01	0.67 ± 0.08	5.30 ± 0.26
PST 1% Co	408.9 ± 15	0.43 ± 0.02	0.50 ± 0.02	5.30 ± 0.25

membranes. The decrease in the surface area for the PST 1% Co sample was due to the increase in the crystallite anatase size from 16.7 to 17.2 nm of TiO_2 flattened bars particles. The relationship of specific surface area with crystallite anatase size was determined for each of the samples. The PST sample showed a ratio of 20.88 $m^2\ nm^{-1}\ g^{-1}$, while 32.10 $m^2\ nm^{-1}\ g^{-1}$ was obtained for the PST 0.5% Co sample and 27.77 $m^2\ nm^{-1}\ g^{-1}$ for PST 1% Co. The size-volume ratio results better for the finest spherical-like assembly, the surface decreases without cobalt incorporation and with the increase of cobalt content due to more intensity of rutile and anatase diffraction peak, respectively. This phenomenon is due to the emergence of Si–O network that inhibits to certain extend the formation of anatase TiO_2 crystallites (Fig. 2c). Furthermore, modifying the SiO_2-TiO_2 nanocomposite with cobalt induces the crystallite morphology, due to the presence of proficient cobalt in the PST assembly composite, according to the cobalt loading. These XRD analyses confirm the coexistence of anatase and rutile phases of TiO_2 on the PST assembly, situated on PST 0.5% Co with 536 m^2/g and finest spherical-like assembly. This is reflected in a better spherical-like assembly. Table ST2 in supplementary information shows the relationship of surface area to crystallite size for anatase phase. Waseem et al. [40] mentioned that the decrease in the surface area may be related to the increase in the particle size, which caused the collapse of the pores [40].

The Ostwald ripening followed the oriented attachment growth process in presence of cobalt cations for the formation of flattened bars or nanorods depending on dissolution recrystallization as effect of cobalt incorporation. On the other hand, the Co incorporation produces spherical-like assemblies that increase the amount of mesoporosity due to their particular morphology. These assemblies favor the increase of the surface area and consequently improve the load and release of carvacrol. ICP elemental analyses was carried out to quantify the cobalt content, the doping of nanomaterials consists of seeking to obtain some substitution of the original atoms (Si or Ti) and/or to change the framework, producing defects in the structure during the hydrothermal synthesis step and using loads below 1% by weight. Which is not normally observed by XRD or FTIR due to high dispersion or low concentration. ICP analysis detected 0.01 wt% cobalt in the sample with 1 wt% Co and no cobalt was detected in the case of the sample with 0.5 wt% Co. Incorporation of cobalt cations during PST preparation gives, as a result, the Ostwald ripening, followed by the oriented attachment growth process that leads to the formation of flattened bars or nanorods depending on the dissolution recrystallization as an effect of cobalt incorporation. On the other hand, the initial concentration of Co produces spherical assemblies that increase the amount of mesoporosity due to their special morphology. The case of PST 0.5% Co shows the best spherical assembly effect, which is probably due to the elimination of Co cations during the washing step. This is also good for agricultural or medical applications due to the Co was evacuated or substituting a few Ti or Si atoms so guarantees the biocompatibility of PST-Co materials.

3.4. Load of carvacrol in the SiO_2-TiO_2 composites

Fig. 5a shows the load efficiency for the PST and Co-PST composites and functionalized with triethanolamine, which were kept under darkness for 48 h in the CVC/EtOH solution at room conditions. The efficiency and load capacity were calculated using the Eqs. (1) and (2) in Section 2.4. As observed in the Fig. 5a, the pure composite (PST) had a loading efficiency of 12.6%, followed by the PST 1% Co and PST 0.5% Co, which had values of 12.6% and 11.9%, respectively. After functionalizing with Triethanolamine ($C_6H_{15}NO_3$) the PST samples (with and without Co), the surface of the material became richer and functionalizable due to the high content of OH groups in the TEOA. Consequently, the load efficiency increased from 11 to 12% to 30–37%. The load capacity was 2.1%, 2%, and 2.1% for PST, PST 0.5% Co and PST 1% Co samples respectively. In general, the load efficiency/capacity on SiO_2-TiO_2 was low. While the load capacity of the PST composites functionalized with TEOA was raised from ≈2% (unfunctionalized) to 20–26%, see the Fig. 5b. We believe that the surface modification with triethanolamine helped to increase the load efficiency and load capacity of the PST and Co-PST composites because the diverse OH groups on their surface were linked to the OH groups of the CVC through hydrogen bridges; this, in turn, enhanced the loading of the CVC molecules into the PST architecture.

Fig. 6a shows the FTIR spectra of the PST composites functionalized with triethanolamine (TEOA). As expected, there is an intense band related to OH groups (centered at 3487 cm^{-1}) for all the PST samples functionalized with TEOA. In fact, the PST 1% Co/TEOA sample

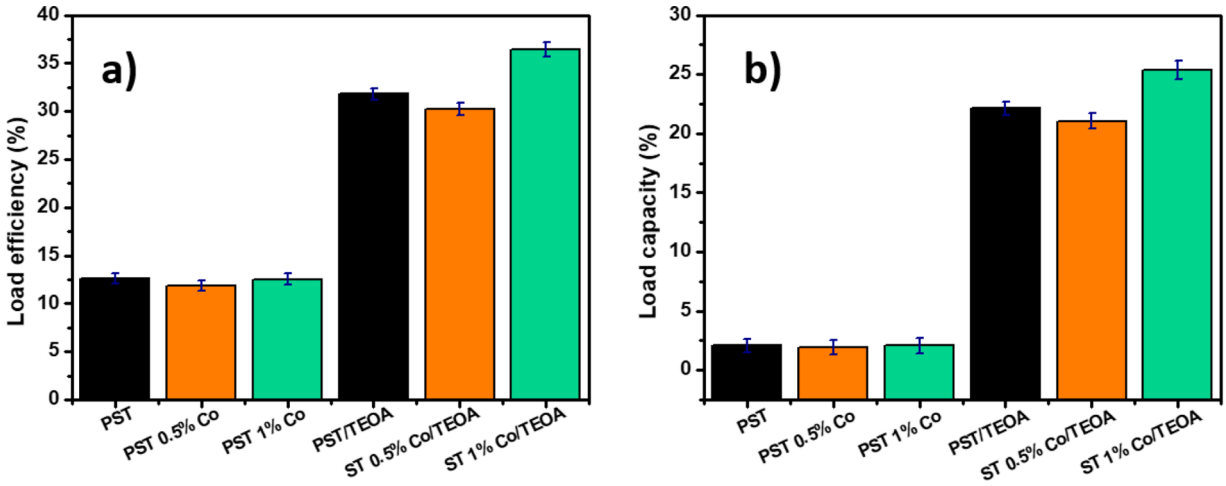

Fig. 5. PST and Co-PST composites and functionalized with triethanolamine (TEOA): a) Load efficiency% and b) Load capacity%.

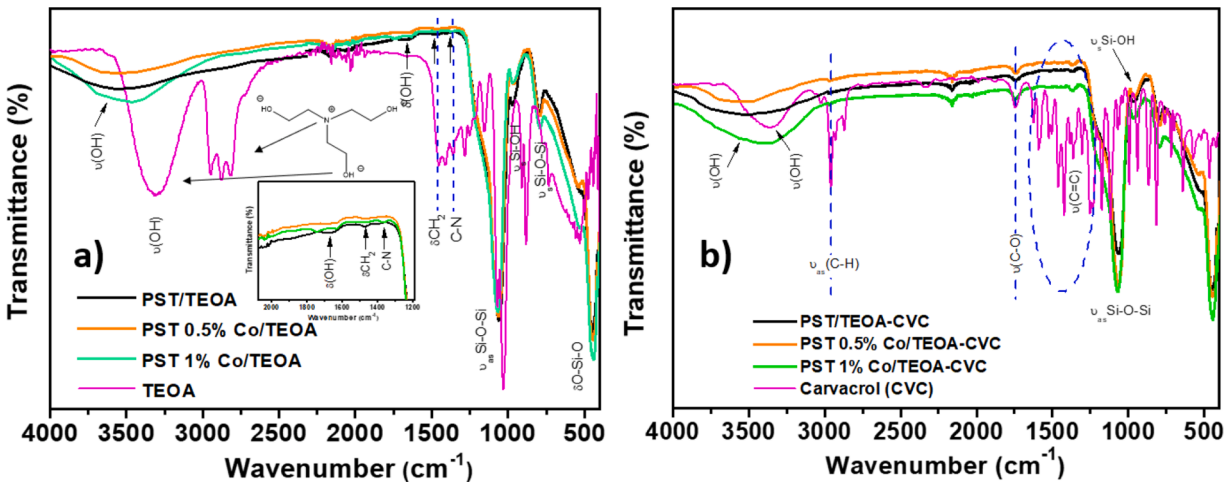

Fig. 6. FTIR spectra for the PST and Co-PST composites functionalized with TEOA: a) before and b) after loading with CVC. The inset in Fig. 6a shows a zoomed view of the 1300–1700 cm^{-1} region.

presented the most intense band centered at 3487 cm^{-1}, the hydroxyl moiety, therefore, this sample presented the highest load efficiency and load capacity (see the Fig. 5b), since a higher content of OH groups promote the formation of hydrogen bridges with CVC. The band observed at 1633 cm^{-1} is attributed to the hydroxyl moiety, while the band at 1467 cm^{-1} is ascribed to the vibrational mode of the CH_2 bond (see inset in Fig. 6b) [41,42]. Also, the band located at 1398 cm^{-1} was attributed to the C—N bond [41,42]; in this case, the ammine was provided by the TEOA. Additionally, we observed the characteristic bands associated to silica and TiO_2 in the range of 450–1350 cm^{-1}. Fig. 6b presents the FTIR spectra of pure CVC, as well as the FTIR spectra for the PST and Co-PST function with TEOA and loaded with CVC. All these samples were functionalized with TEOA. The FTIR spectrum of the pure CVC shows a band at 3354 cm^{-1}, which corresponds to the O—H bonds of phenol. Some vibrational bands corresponding to methyl-methylene -CH_2—CH_3 were observed from 2958 to 2868 cm^{-1}. There are also vibrational bands from 1300 to 1670 cm^{-1} which correspond to C = C/C—O bonds of aromatic compounds [43,44]. If the FTIR spectra of the CVC is compared with the ones corresponding to the PST samples loaded with CVC (PST/TEOA-CVC, PST 0.5% Co/TEOA-CVC and PST 1% Co/TEOA-CVC), we observe three bands centered at 2958, 1739 and 1363 cm^{-1}, which correspond to the asymmetric C—H bond and to the vibrational stretching mode of the C = C/C—O bonds (see the blue dashed line in the Fig. 6b). Thus, the presence of such bands confirmed that the PST samples or doped-Co interacted with functional groups and enhanced the loading with CVC.

3.5. *In-vitro release of carvacrol*

Fig. 7a shows the release kinetics for the PST and Co-PST composites. The cumulative release of CVC was analyzed at pH 3.0 and 7.4. It was observed that the pH and solubility of CVC influenced the release rate of CVC in the SiO_2-TiO_2 composites. The PST-CVC, PST 0.5% Co-CVC and the PST 1% Co-CVC samples in an acid medium presented cumulative release (after 60 min and 30 min for Co-PST) of 19.3%, 17.4%, and 17.9%, respectively. After this, a constant release was achieved from the 2 h to 24 h in the three composites. At the pH=7.4, the maximum release percentage (18.3%) occurred after 60 min for the PST-CVC sample, while the maximum release of 23.1% and 28.9% occurred for the PST 0.5% Co-CVC and PST 1% Co-CVC samples, respectively, after 24 h. This means that a neutral pH maximized the release of the CVC and the amount of CVC released is the highest for the sample made with 1 wt% of Co.

Fig. 7b shows the release kinetics of CVC for the PST composites functionalized with TEOA. If we compare these plots with the corresponding ones in the Fig. 7a, we observed an increment of the release% of carvacrol for all the samples and for any pH (3.0 or 7.4). Thus, modifying the surface of the PST composites with TEOA not only helped

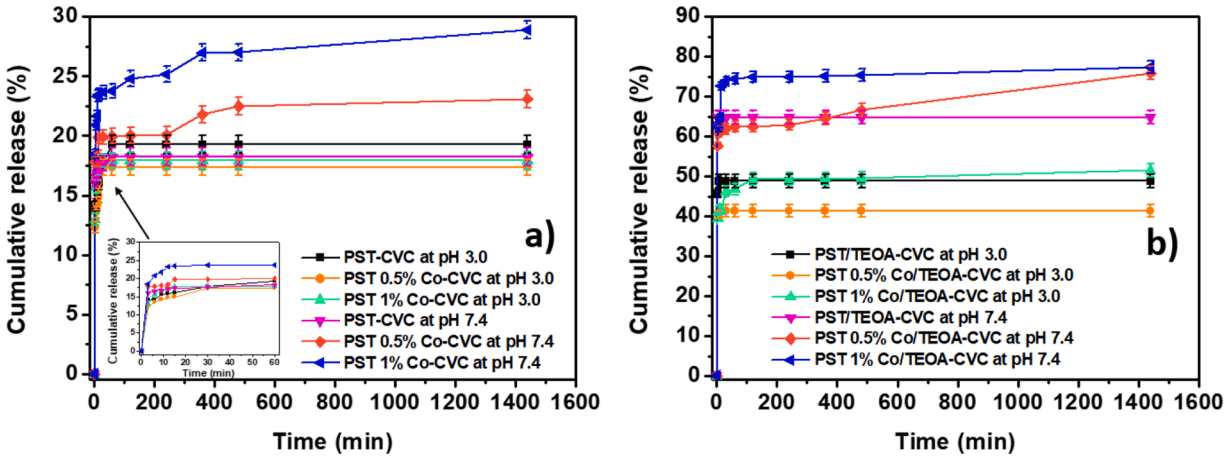

Fig. 7. Carvacrol (CVC) release kinetics for the PST and Co-PST composites using the pH values of 3 and 7.4: a) without functionalization with TEOA and b) functionalized with TEOA.

to have a higher loading capacity, but also to increase the release% compared to the composites without functionalization. The release of the PST composites modified with triethanolamine and loaded with CVC at pH 3.0 were 48.8%, 41.4% and 51.5% for the PST/TEOA-CVC, PST 0.5% Co/TEOA-CVC and PST 1% Co/TEOA-CVC samples, respectively. Those maximal release% were reached after 6 min, 12 min and 24 h for the PST/TEOA-CVC, PST 0.5% Co/TEOA-CVC and PST 1% Co/TEOA-CVC samples, respectively. At a pH=7.4 the PST/TEOA-CVC, PST 0.5% Co/TEOA-CVC and PST 1% Co/TEOA-CVC samples released 64.8% in 3 min, 75.9% in 24 h and 77.4% in 24 h, respectively. Based on the above results, we observe that the sample PST without Co released quickly a high amount of CVC (at neutral pH), while the samples made with the Co had a slower release of CVC and higher releases% were reached as well. In fact, the sample doped with 1 wt% of Co and functionalized with TEOA presented the highest amount of CVC released. We believe that the release% was low at acidic conditions due to the following reasons [45]: At acidic conditions, we have an excess of protons (H^+) in the aqueous medium, which causes a low solubility of the CVC, therefore, its dissociation to be released is diminished. At higher pH values, the content of ionic species is high (OH^-radicals), which facilitates the dissociation of the CVC molecules, and this gives rise to their easy release from the mesopores where they are stored.

3.6. Carvacrol release profiles

In order to better understand the release mechanism of carvacrol (CVC) in SiO_2-TiO_2 composites without and Co-doped, as well as composites surface-modified with triethanolamine (TEOA), the data experimental were fitted using several law models as zero order, first order, Higuchi, Hixson-Crowell and Korsmeyer-Peppas [46,47]. The equations of the mathematical models are found in the supporting information.

Table 2 summarizes the parameters of the release kinetics of the SiO_2-TiO_2 composites without and Co-doped at pH 3.0 and 7.4. It was observed that the PST-CVC, PST 0.5% Co-CVC, and PST 1% Co-CVC composites at pH 3.0 showed low correlation coefficients (R^2) <0.5, indicating that the obtained data cannot be fitted with the available mathematical models. However, in the Korsmeyer-Peppas model, it was observed that the release kinetics follows two behaviors, so the linear adjustment has been made separately for each behavior, obtaining correlation coefficients >0.90. This indicates that the kinetic data follow the Korsmeyer-Peppas model. Also, the values of n and k have been determined based on the Korsmeyer-Peppas equation. In the case of PST-CVC at pH 3.0, a n value of 0.1106 and a k value of 1.0827 min^{-n} was obtained with a correlation coefficient of 0.9605. For PST 0.5% Co-CVC the values of n and k were 0.1429 and 1.0186, respectively with a R^2 of 0.9773. While, for the PST 1% Co-CVC sample, a n value of 0.1957 and a k value of 1.0295 were obtained. On the other hand, the evaluation of the zero order, first order, Higuchi, Hixson-Crowell models in the PST-CVC composites at pH 7.4 showed correlation coefficients less than 0.5. However, with the Korsmeyer-Peppas model, an R^2 value of 0.8604 was obtained. In the same way, two behaviors have been noticed. So, when making the adjustment, R^2 value of 0.9925 was obtained with an n value of 0.0425 and 1.1863 as the value of k. While for the PST composites with 0.5% and 1% Co, n values of 0.0427 and 0.0587 were obtained, respectively. The k values were 1.2246 and 1.277 for PST 0.5% Co-CVC and PST 1% Co-CVC, respectively. For the PST 0.5% Co-CVC and PST 1% Co-CVC composites at pH 7.4, the release kinetics follows the Korsmeyer-Peppas model, as indicated by the higher R^2 values, of 0.8865 and 0.8933, respectively.

Therefore, we conclude that the kinetics of the PST composites at pH 3.0 and 7.4 follows the Korsmeyer-Peppas model and therefore the release occurs by the Fick mechanism since the value of n is less than 0.45. Figure S4 in the supporting information shows the fit of the curves for each of the PST composites.

Table 3 summarizes the release kinetics parameters of the TEOA-modified SiO_2-TiO_2 composites without Co and with cobalt at pH 3.0 and 7.4. The release kinetics of the PST/TEOA-CVC, PST 0.5% Co/TEOA-CVC and PST 1% Co/TEOA-CVC composites at pH 3.0 follow

Table 2
Release kinetics parameters of carvacrol from SiO_2-TiO_2 composites.

Sample name	pH	Correlation coefficient (R^2)						k (min^{-n})	n
		Zero order	First order	Higuchi	Hixson-Crowell	Korsmeyer-Peppas	Two behaviors		
PST-CVC	3.0	0.2581	0.2596	0.5003	0.2591	0.8758	0.9605	1.0827	0.1106
PST 0.5% Co-CVC	3.0	0.2016	0.2027	0.4087	0.2023	0.7914	0.9773	1.0186	0.1429
PST 1% Co-CVC	3.0	0.0921	0.0932	0.2039	0.0928	0.4867	0.9668	1.0295	0.1957
PST-CVC	7.4	0.2359	0.2367	0.4651	0.2364	0.8604	0.9925	1.1863	0.0425
PST 0.5% Co-CVC	7.4	0.6269	0.6346	0.8199	0.632	0.8865	—	1.2246	0.0427
PST 1% Co-CVC	7.4	0.571	0.5909	0.7732	0.5843	0.8933	—	1.277	0.0587

Table 3
Telease kinetics parameters of carvacrol from SiO_2-TiO_2 composites modified with TEOA.

Sample name	pH	Correlation coefficient (R^2)					k (min^{-n})	n
		Zero order	First order	Higuchi	Hixson-Crowell	Korsmeyer-Peppas		
PST/TEOA-CVC	3.0	0.0304	0.0304	0.0734	0.0304	0.2589	1.1587	0.2513
PST 0.5% Co/TEOA-CVC	3.0	0.0853	0.0854	0.1894	0.0854	0.8444	1.5987	0.0155
PST 1% Co/TEOA-CVC	3.0	0.4471	0.4657	0.702	0.4595	0.9286	1.5804	0.0454
PST/TEOA-CVC	7.4	0.0257	0.0257	0.0802	0.0257	0.2523	1.2503	0.2665
PST 0.5% Co/TEOA-CVC	7.4	0.9369	0.9597	0.8904	0.9539	0.7064	1.752	0.0286
PST 1% Co/TEOA-CVC	7.4	0.2953	0.3328	0.4964	0.3195	0.7479	1.7858	0.0372

the Korsmeyer-Peppas model with correlation coefficients of 0.2589, 0.8444 and 0.9286, respectively. The *k* values were 1.1587, 1.5987, and 1.5804, while the n values were 0.2513, 0.0155, and 0.0454 for PST/TEOA-CVC, PST 0.5% Co/TEOA-CVC, and PST 1% Co/TEOA-CVC, respectively. So, diffusion occurs by the mechanism of Fick. In the case of the composites at pH 7.4, it was observed that the PST/TEOA-CVC and PST 1% Co/TEOA-CVC composites follow the Korsmeyer-Peppas model with an *n* value of 0.2665 and 0.0372, respectively. Since the value of *n* is less than 0.45, the release of carvacrol in the composites occurs through Fick diffusion. While the release kinetics of the PST 0.5% Co/TEOA-CVC composite follows the first order model with a correlation coefficient of 0.9597 which indicates that the rate is directly proportional to the concentration of carvacrol in the dissolution medium. Figure S5 in the supporting information shows the fitting of the curves for each of the PST and Co-PST composites surface modified with TEOA.

On the other hand, the Korsmeyer-Peppas model has been widely used to model the release kinetics of drugs such as Khellin and Doxycycline in mesoporous materials such as functionalized aluminosilicate nanoparticles, also known as halloysite nanotubes [48,49].

For applications in agriculture, a slow release of the antibacterial molecule is needed since we want to protect the crops for long times while maximizing the amount of released carvacrol. Thus, the PST 1% Co/TEOA-CVC sample could be useful for agricultural applications. Agricultural evaluation normally takes place at a pH of natural water close to 6.5–7.0, but also there is a detrimental effect mainly in over-fertilized hydroponic cultivation that acidifies the water. Thus, the study at pH 3.0 to test in acid conditions gives insights of release kinetics under such conditions.

4. Conclusions

In this research, we reported a practical method for the synthesis of mesoporous SiO_2-TiO_2 composites with high surfaces areas of 391–537 $m^2\ g^{-1}$. Those composites present an architecture with spherical-like assembly of flattened bars and nanorods. In fact, the size of the nanorods increased from 83 to 95 nm after increasing the initial Co concentration from 0.5 to 1 wt% in the composites. PST composites also presented a mixture of anatase and rutile phases according to the analysis by X-ray diffraction. The performance of such composites was studied for the loading of the carvacrol as antibacterial model molecule. Despite their high surface area, the PST composites presented low load efficiencies of 11–13%, but it was raised to 30–37% after the functionalization of the PST composites with the TEOA. The release% of the CVC herbicide was also evaluated under acidic and neutral conditions. Subsequently, the PST composites were functionalized with the TEOA and their release% was calculated again under acidic and basic conditions. In general, the longest delivery times and the highest loading/delivery percentages were observed for the PST sample synthesized with 1 wt% of Co and functionalized with TEOA. The undoped PST sample (with or without TEOA functionalization) released a maximum amount of CVC in a few minutes. In contrast, the samples synthesized with Co presented longer delivery times of 24 h.

It is worthy to notice that functionalizing the composites with the TEOA provided OH groups to their surface that facilitated the linkage of the CVC molecules (through hydrogen bonds) and this enhanced the storage area of the CVC into the PST composites. Hence, the results of this investigation demonstrate that the functionalization of the composites with TEOA is a good strategy to increase the loading of herbicides and to prolong their delivery time (24 h or more), which is of current interest for the application of nanomaterials in the agriculture, since they could be used for the control of unwanted plants and phytopathogens in crops.

CRediT authorship contribution statement

T.A. Esquivel-Castro: Methodology, Investigation, Validation, Formal analysis, Writing – original draft. **G. Robledo-Trujillo:** Methodology, Investigation, Validation. **J. Oliva:** Data curation, Resources, Writing – review & editing. **H.C. Rosu:** Resources, Writing – review & editing. **V. Rodríguez-González:** Conceptualization, Project administration, Writing – review & editing.

Declaration of Competing Interest

The authors declare that they have no known competing financial interests or personal relationships that could have appeared to influence the work reported in this paper.

Data availability

Data will be made available on request.

Acknowledgments

T. A. Esquivel-Castro thanks CONACyT-Mexico for the postdoctoral scholarship. We also appreciate the technical support for the SEM, XRD and SAXS measurements to Ana Iris Peña Maldonado, Beatriz Rivera Escoto and Ignacio Becerril performed in LINAN-IPICYT. V. Rodríguez-González also acknowledges the financial support by the CONACyT, Ciencia de Frontera Project 101703.

Supplementary materials

Supplementary material associated with this article can be found, in the online version, at doi:10.1016/j.apsadv.2023.100378.

References

[1] M. Murali, H. Gowtham, S. Singh, N. Shilpa, M. Aiyaz, M. Alomary, M. Alshamrani, A. Salawi, Y. Almoshari, M. Ansari, K. Amruthesh, Fate, bioaccumulation and toxicity of engineered nanomaterials in plants: current challenges and future prospects, Sci. Total Environ. 811 (2022), 152249.
[2] R. Hamers, Nanomaterials and global sustainability, Acc. Chem. Res. 50 (2017) 633–637.
[3] T. Ahmed, M. Noman, M. Ijaz, S. Ali, M. Rizwan, U. Ijaz, A. Hameed, U. Ahmad, Y. Wang, G. Sun, B. Li, Current trends and future prospective in nanoremediation of heavy metals contaminated soils: a way forward towards sustainable agriculture, Ecotoxicol. Environ. Saf. 227 (2021), 112888.

[4] M. Arham, H. Zia, M. Zeeshan, M. Khan, M. Shahid, Metal organic frameworks (MOFs) as a cutting-edge tool for the selective detection and rapid removal of heavy metal ions from water: recent progress, J. Environ. Chem. Eng. 10 (2022), 106991.

[5] Z. Ren, L. Wang, Y. Li, J. Zha, G. Tian, F. Wang, H. Zhang, J. Liang, Synthesis of zeolites by in-situ conversion of geopolymers and their performance of heavy metal ion removal in wastewater: a review, J. Clean. Prod. 349 (2022), 131441.

[6] A. Gutierrez, R. Nomen, J. Sempere, J. Parra, M. Montes, R. Gonzalez, A fast methodology to rank adsorbents for CO_2 capture with temperature swing adsorption, Chem. Eng. J. 435 (2022), 134703.

[7] H. Yan, G. Zhang, Y. Xu, Q. Zhang, J. Liu, G. Li, Y. Zhao, Y. Wang, Y. Zhang, High CO_2 adsorption on amine-functionalized improved macro-/mesoporous multimodal pore silica, Fuel 315 (2022), 123195.

[8] Y. Mochizuki, J. Bud, E. Byambajav, N. Tsubouchi, Influence of ammonia treatment on the CO_2 adsorption of activated carbon, J. Environ. Chem. Eng. 10 (2022), 107273.

[9] E. Cueto, F. Suárez, S. Gálvez, M. Valles, E. Mateo, CO_2 adsorption capacities of amine-functionalized microporous silica nanoparticles, React. Funct. Polym. 170 (2022), 105100.

[10] A. Avellan, J. Yun, B. Morais, E. Clement, S. Rodrigues, G. Lowry, Critical review: role of inorganic nanoparticle properties on their foliar uptake and in planta translocation, Environ. Sci. Technol. 55 (2021) 13417–13431.

[11] Y. Wang, C. Deng, S. Rawat, K. Cota, I. Medina, J. Gardea, Evaluation of the effects of nanomaterials on rice (Oryza sativa L.) responses: underlining the benefits of nanotechnology for agricultural applications, ACS Agric. Sci. Technol. 1 (2021) 44–54.

[12] N. Scott, H. Chen, H. Cui, Nanotechnology applications and implications of agrochemicals toward sustainable agriculture and food systems, J. Agric. Food Chem. 66 (2018) 6451–6456.

[13] S. Shekhar, S. Sharma, A. Kumar, A. Taneja, B. Sharma, The framework of nanopesticides: a paradigm in biodiversity, Mater. Adv. 2 (2021) 6569–6588.

[14] L. Zhao, L. Lu, A. Wang, H. Zhang, M. Huang, H. Wu, B. Xing, Z. Wang, R. Ji, Nano-biotechnology in agriculture: use of nanomaterials to promote plant growth and stress tolerance, J. Agric. Food Chem. 68 (2020) 1935–1947.

[15] X. Cao, L. Yue, C. Wang, X. Luo, C. Zhang, X. Zhao, F. Wu, J. White, Z. Wang, B. Xing, Foliar application with Iron Oxide nanomaterials stimulate nitrogen fixation, yield, and nutritional quality of soybean, ACS Nano 16 (2022) 1170–1181.

[16] A. Gogos, K. Knauer, T. Bucheli, Nanomaterials in plant protection and fertilization: current state, foreseen applications, and research priorities, J. Agric. Food Chem. 60 (2012) 9781–9792.

[17] A. Sikder, A. Pearce, S. Parkinson, R. Napier, R. O'Reilly, Recent trends in advanced polymer materials in agriculture related applications, ACS Appl. Polym. Mater. 3 (2021) 1203–1217.

[18] C. Natal, M. Fernandes, N. Pinto, R. Pereira, T. Vieira, A. Rodrigues, D. Pereira, S. Sousa, A. Fortes, E. Castanheira, M. Goncalves, New carvacrol and thymol derivatives as potencial insecticides: synthesis, biological activity, computational studies and nanoencapsulation, RSC Adv. 11 (2021) 34024–34035.

[19] A. Asfaram, H. Sadeghi, A. Goudarzi, E. Kokhdan, Z. Salehpour, Ultrasound combined with manganese-oxide nanoparticles loaded on activated carbon for extraction and pre-concentration of thymol and carvacrol in methanolic extracts of Thymus daenensis, Salvia officinalis, Stachys pilifera, Satureja khuzistanica, Analyst 144 (2019) 1923–1934.

[20] S. Rao, G. Xu, H. Zeng, X. Zheng, Q. Hu, Q. Wang, Z. Yang, X. Jiao, Physicochemical and antibacterial properties of fabricated ovalbumin-carvacrol gel nanoparticles, Food. Funct. 11 (2020) 5133–5141.

[21] M. Friedman, Chemistry and multibeneficial bioactivities of carvacrol (4-Isopropyl-2-methylphenol), a component of essential oils produced by aromatic plants and spices, J. Agric. Food Chem. 62 (2014) 7652–7670.

[22] S. Armorini, J. Yeatts, K. Mullen, S. Mason, E. Mehmeti, K. Anderson, S. Washburn, R. Baynes, Development of a HS-SPME-GCMS–/MS method for the quantitation of thymol and carvacrol in bovine matrices and to determine residue depletion in milk and tissues, J. Agric. Food Chem. 64 (2016) 7856–7865.

[23] A. Altan, Ö. Cayir, Encapsulation of carvacrol into ultrafine fibrous zein films via electrospinning for active packaging, Food Packag. Shelf Life 26 (2020), 100581.

[24] M. Luna, O. Beltran, D. Encinas, M. Ballesteros, A. Topete, N. Hassan, M. López, V. Reyes, M. Valdez, J. Juarez, High antibacterial performance of hydrophobic chitosan-based nanoparticles loaded with carvacrol, Colloids Srf. B: Biointerfaces 209 (2022), 112191.

[25] A. Salari, K. Roshanaei, B. Rasoulian, J. Khalili, Carvacrol loaded beta cyclodextrin-alginate-chitosan based nanoflowers attenuates renal toxicity induced by malathion and parathion: a comparative toxicity, Pestic. Biochem. Phys. 172 (2021), 104747.

[26] R. Kumar, Y. Han, H. Xia, S. Wang, A. Chen, Nanoarchitectured prototypes of mesoporous silica nanoparticles for innovative biomedical applications, J. Nanobiotechnology 20 (2022) 126.

[27] V. Rodríguez, S. Obregón, O. Patrón, C. Terashima, A. Fujishima, An approach to the photocatalytic mechanism in the TiO_2-nanomaterials microorganism interface for the control of infectious processes, Appl. Catal. B 270 (2020), 118853.

[28] W. Nong, W. Guan, Y. Yin, C. Lu, Q. Wang, Y. Luo, B. Zhang, Z. Xu, J. Wu, Y. Guan, Photo-triggered on-demand carvacrol vapor release from nano-generators for non-contact bacterial inactivation between nanomaterials and bacteria, Chem. Eng. J. 420 (2021), 129874.

[29] N. Basiron, S. Sreekantan, H. Akil, K. Saharudin, N. Harun, R. Mydin, A. Seeni, N. Abdul, F. Adam, A. Iqbal, V. Kumaravel, Effect of Li-TiO_2 nanoparticles incorporation in LDPE polymer nanocomposites for biocidal activity, Nano-Struct. Nano-Objects 19 (2019), 100359.

[30] X. Su, Z. Wang, Y. Huang, Z. Miao, S. Wang, J. Wang, X. Zhang, X. Sun, H. Liu, Y. Sang, Triethanolamine interface modification of crystallized ZnO nanospheres enabling fast photocatalytic hazard-free treatment of Cr(VI) ions, Nanotechnol. Rev. 10 (2021) 847–856.

[31] H. Hamad, M. El-Latif, A. Kashyout, W. Sadik, M. Feteha, Synthesis and characterization of core-shell-shell magnetic ($CoFe_2O_4$-SiO_2-TiO_2) nanocomposites and TiO_2 nanoparticles for the evaluation of photocatalytic activity under UV and visible irradiation, New J. Chem. 39 (2015) 3116–3128.

[32] V. Mesilov, V. Galakhov, A. Gubkin, E. Sherstobitova, G. Zakharova, M. Uimin, A. Yermakov, K. Kvashnina, D. Smirnov, X-ray diffraction and X-ray spectroscopy studies of cobalt-doped anatase TiO_2:co nanopowders, J. Phys. Chem. C 121 (2017) 24235–24244.

[33] H. Pérez, R. Miranda, Z. Saavedra, R. Zarraga, P. Alonso, E. Moctezuma, J. Martínez, Green and facile sol-gel synthesis of the mesoporous SiO_2-TiO_2 catalyst by four different activation modes, RSC Adv 10 (2020) 39580–39588.

[34] R. Al-Oweini, H. El-Rassy, Synthesis and characterization by FTIR spectroscopy of silica aerogels prepared using several $Si(OR)_4$ and R''$Si(OR')_3$ precursors, J. Mol. Struct. 919 (2009) 140–145.

[35] S. Warring, D. Beattie, A. McQuillan, Surficial siloxane-to-silanol interconversion during room-temperature hydration/dehydration of amorphous silica films observed by ATR-IR and TIR-Raman spectroscopy, Langmuir 32 (2016) 1568–1576.

[36] J. Iturbe-Ek, J. Andrade, R. Gómez, V. Rodríguez, A functional assembly of SiO_2 nanospheres/graphene oxide composites, Mater. Lett. 142 (2015) 75–79.

[37] K. Sing, D. Everett, R. Haul, L. Moscou, R. Pierotti, J. Rouquérol, T. Siemieniewska, Reporting physisorption data for gas/solid systems with special reference to the determination of surface area and porosity, Pure & Appl. Chem. 4 (1985) 603–619.

[38] S. Bepari, X. Li, R. Abrokwah, N. Mohammad, M. Arslan, D. Kuila, Co-Ru catalysts with different composite oxide supports for Fischer-Tropsch studies in 3D-printed stainless steel microreactors, Appl. Catal. A-Gen. 608 (2020), 117838.

[39] Z. Pan, X. Zhu, H. Jiang, Y. Liu, R. Chen, Flexible hierarchical Pd/SiO_2-TiO_2 nanofibrous catalytic membrane for complete and continuous reduction of p-nitrophenol, J. Exp. Nanosci 16 (2021) 62–80.

[40] M. Waseem, S. Muntha, M. Nawaz, W. Rehman, M. Rehman, K. Shah, Effect of heat treatment on the efficient adsorption of Cd^{2+} ions by nanosized SiO_2, TiO_2 and their composite, Mater. Res. Express 4 (2017), 015017.

[41] X. Zhang, P. Jin, D. Xu, J. Zheng, Z. Zhan, Q. Gao, S. Yuan, Z. Xu, B. Van der Bruggen, Triethanolamine modification produces ultra-permeable nanofiltration membrane with enhanced removal efficiency of heavy metal ions, J. Membr. Sci. 644 (2022), 120127.

[42] G. Sippel, P. Braga, K. Dias de Freitas, F. Wypych, S. Nakagaki, Catalysts for heterogeneous oxidation reaction based on metalloporphyrins immobilized on kaolinite modified with triethanolamine, J. Colloid Interface Sci. 374 (2012) 278–286.

[43] D. Berraaouan, M. Elmiz, K. Essifi, S. Salhi, A. Tahani, Adsorption of carvacrol on modified bentonite in aqueous solutions, Mater. Today Proc. 31 (2020) S28–S32.

[44] Z. Taghizadeh, S. Rakhshani, V. Jahani, O. Rajabi, H. Haghighi, M. Abbaspour, Preparation and in vitro characterization of carvacrol pellets by combination of liquisolid technique and extrusion-spheronization, J. Drug Deliv. Sci. Technol. 61 (2021), 102232.

[45] O. Cediilo, N. Rodríguez, A. Hipólito, D. Nivón, R. Gómez, R. Moya, Effect of the pH on the thermodynamic stability of inclusion complex of thymol and carvacrol in B-cyclofextrin in water, Food Hydrocoll 124 (2022), 107307.

[46] R. Gaglio, L. Botta, G. Garofalo, A. Miceli, L. Settanni, F. Lopresti, Carvacrol activated biopolymeric foam: an effective packaging system to control the development of spoilage and pathogenic bacteria on sliced pumpkin and melon, Food Packag. Shelf Life 28 (2021), 100633.

[47] R. Gouda, H. Baishya, Z. Qing, Application of mathematical models in drug release kinetics of carbidopa and levodopa ER tablets, J. Develop Drugs 6 (2017) 1–8.

[48] L. Lisuzzo, G. Cavallaro, S. Milioto, G. Lazzara, Halloysite nanotubes coated by chitosan for the controlled release of Khellin, Polymers (Basel) 12 (2020) 1766.

[49] G. Cavallaro, G. Lazzara, S. Milioto, F. Parisi, V. Evtugyn, E. Rozhina, R. Fakhrullin, Nanohydrogel formation within the halloysite lumen for triggered and sustained release, ACS Appl. Mater. Interfaces 10 (2018) 8265–8273.